# Analysis of the Cavitating Draft Tube Vortex in a Francis Turbine Using Particle Image Velocimetry Measurements in Two-Phase Flow

**Monica Sanda Iliescu**
Dr. Ing.
Assistant
e-mail: msiliescu@yahoo.fr

**Gabriel Dan Ciocan**
Dr. Ing.
Research Associate
e-mail: gabrieldan.ciocan@orange.fr

**François Avellan**
Dr. Ing.
Professor
e-mail: francois.avellan@epfl.ch

Laboratory for Hydraulic Machines,
Ecole Polytechnique Fédérale de Lausanne
(EPFL),
Avenue de Cour 33bis,
CH-1007 Lausanne, Switzerland

*Partial flow rate operation of hydroturbines with constant pitch blades causes complex unstable cavitating flow in the diffuser cone. A particle image velocimetry (PIV) system allows investigating the flow velocity field in the case of a developing cavitation vortex, the so-called vortex rope, at the outlet of a Francis turbine runner. The synchronization of the PIV flow survey with the rope precession allows applying the ensemble averaging by phase technique to extract both the periodic velocity components and the rope shape. The influence of the turbine setting level on the volume of the cavity rope and its center-line is investigated, providing a physical knowledge about the hydrodynamic complex phenomena involved in the development of the cavitation rope in Francis turbine operating regimes.* [DOI: 10.1115/1.2813052]

## 1 Introduction

For hydraulic turbines, the operating points at partial flow rate are associated with a vortex at the runner outlet, in the draft tube cone. Cavitation develops into the low pressure zone of the vortex core, see Fig. 1. The vortex rope, a helical vortex that is cavitating in its core, appears and the cavitating volume varies with the underpressure level. The rope frequency depends on the $\sigma$ level and if it comes close to one of the eigenfrequencies of the turbine or associated circuit, the resonance phenomenon may appear. The unsteady fluctuations can be amplified and lead to important damage. Jacob [1] presents a review of the effects of this operating regime on the power plant operation.

A first approach is to model the rope phenomenology. Different models are proposed. Arndt [2] makes a synthesis of the classical approaches by defining a swirl parameter to characterize the vortex rope—called the hub vortex. Qualitative correlations between the swirl number and flow visualization or pressure measurements seem to be in good agreement.

Alekseenko et al. [3] present experiments of axisymmetrical vortices in a vertical vortex chamber with tangential supply of liquid through turning nozzles. They give an analytical solution of an elementary cylindrical vortex structure considered like an infinitely thin filament, accounting for the helical shape of the vortex lines. Different laws of vorticity distribution and finally a formula for the calculation of the self-induced velocity of helical vortex rotation (precession) in a cylindrical tube is given. Okulov [4] extends this approach to a conical vortex, for a small cone opening angle. Validations are not available for this approach, and the cone angle limitation is a strong constraint in applying this model to turbine vortex ropes.

Wang et al. [5] propose two mathematical models: a partially rolled-up vortex for predicting the rope frequency and a "spiral cone cavity" for predicting the cavitation volume in the draft tube. The results are compared with the wall pressure measurements and qualitatively with rope visualizations.

Philibert and Couston [6] propose a hydroacoustic model, and the rope is represented by a pipe characterized by its length, wave celerity, and a coefficient related to the rope radius variation with the discharge. The $\sigma$ influence is neglected and experimental data are needed for the model calibration.

Hocevar et al. [7] use radial basis neural networks to predict the vortex rope dynamics in a Francis turbine. The pressure spectrum is well predicted and the void fraction corresponds qualitatively to the experimental estimation. However, the method depends on the learning set and cannot predict the unstable behavior of the rope.

Zhang et al. [8], starting from Reynold's averaged Navier-Stokes (3D RANS) numerical simulations, and Susan-Resiga et al. [9], starting from a theoretical analysis of experimental data, show that the rope origin is the absolute instability of the swirling flow at the cone inlet of the turbine draft tube. However, the rope evolution in the cone is predicted only from the point of view of its stability.

A second approach, made possible by the increase of computers' power and of the ability of CFD codes to simulate the complex flow behavior, is the numerical simulation of the rope phenomenology. The state of the art in the numerical computation for the cavitation-free configuration is presented by Ciocan et al. [10]. They show, for the rope configuration in cavitation-free conditions, that the RANS calculation can give very accurate results, but a detailed validation is necessary before using the CFD codes for design purposes. More complex numerical investigations are presented by Paik et al. [11], comparing unsteady Reynold's averaged Navier-Stokes (3D URANS) and direct numerical simulation (3D DNS) numerical simulations in a hydraulic turbine draft tube. Globally, the phenomenology is well predicted, but discrepancies persist in the turbulence and vortex structures in the straight diffuser downstream of the elbow. Once more, the need for detailed flow measurements to improve the draft tube phenomenology modeling is mentioned by the authors.

These approaches are based on a series of hypotheses for the rope phenomenology, which are not yet verified experimentally. Therefore, detailed measurements of the rope volume and the associated velocity fields, in addition to classical wall pressure and torque measurements, are of prime importance for quantitative
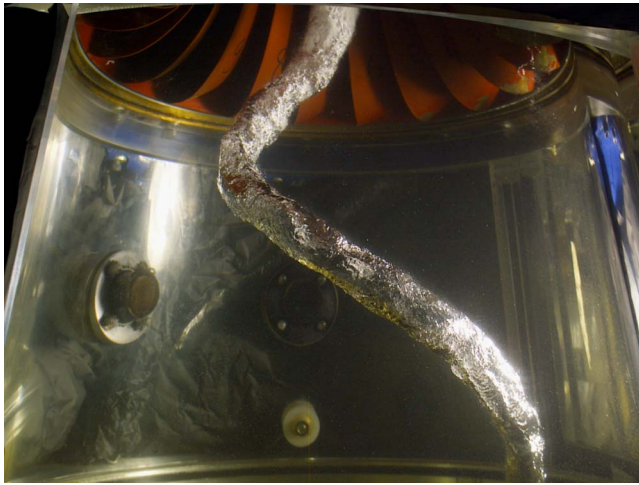
Fig. 1 Development of the vapor core rope for $\sigma=0.380$



Fig. 2 Francis turbine scale model

validation. An extension of the investigation is necessary in order to demonstrate the $\sigma$ influence and/or the turbine-circuit interaction influence on the rope phenomenology.

Particle Image Velocimetry (PIV) is a well established technique, see Adrian [12]. Recently, the PIV measurement technique has been applied for two-phase flows, as well in liquid-solid flows—see Kadambi et al. [13]—as in liquid-air flows (bubbly flows).

Dias and Riethmuller [14] used the PIV technique to investigate air bubbles injected into stagnant water. They measured the flow field induced by a single bubble in a water tank by means of 2D PIV, along with the contour of the bubble by the shadow detection method. If the same image is used to obtain the velocity field and the bubble contour, an error of 40% is observed for the bubble contour due to the mirror effect of the bubble boundary. Using fluorescent particles and a high-pass filter, an uncertainty of 3% for the bubble size and velocity, and 2.5% for liquid velocity at 75% confidence level, is obtained.

Lindken and Merzkirch [15] performed the reconstruction of the 3D position and volume of bubbles rising in a pipe, along with the 2D velocity field of the liquid phase. The experimental setup is made of two perpendicular laser sheets of different wavelengths, and two cameras focused on the corresponding laser sheet. The bubble sizes are evaluated from their projections on both laser sheets. Using a $532 \pm 1.5$ nm filter on the PIV camera, they obtained an uncertainty of 2% for the liquid velocity, 10% for the bubble shape, 5% for the bubble center, and 8% for the bubble velocity, after the rejection by a particular filtering technique of 3–5% of the images due to strong reflections. Next, Lindken and Merzkirch [16] improved this measurement method by combining three different techniques: PIV with fluorescent particles, shadowgraphy, and digital phase separation. In this way, they characterize the local modification of the turbulence in the liquid phase by the bubble passage.
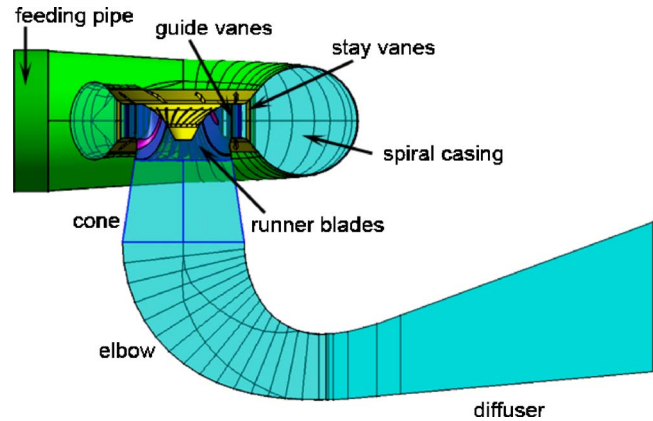
Starting from these applications, we developed a PIV two-phase application that enables simultaneous measurements of the flow velocity field and the volume of a compact unsteady vapor cavity—the rope. Specific image acquisition and filtering procedures are implemented for the investigation of cavity volume and its evolution related to the underpressure level in the draft tube. For the first time, the development of the rope in the diffuser cone of a Francis turbine scale model is quantified.

One operating point is selected at partial flow rate operating conditions: for $\psi=1.18$ and $\varphi=0.26$, which corresponds to about 70% $Q_{BEP}$. To investigate the influence of the cavity size, the Thoma cavitation number is decreased from $\sigma=1.18$, cavitation-free condition, to $\sigma=0.38$, maximum rope volume, considering seven $\sigma$ values. For the extreme values of $\sigma$, nine phases are acquired in order to reconstruct the rope shape by the ensemble averaging by phase technique. The measurement conditions are summarized in Table 1.

## 2 Scale Model of the Francis Turbine

In a Francis turbine, see Fig. 2, the flow incoming from the feed pipe is uniformly distributed along the runner inlet circumference by a spiral casing with gradually decreasing cross section. A first row of stay vanes ensures the mechanical resistance of the assembly, while a second row, of adjustable guide vanes, provides the optimum incidence angle to the flow at the runner's periphery and adjusts the turbine flow rate.

The kinetic energy of the water is then transformed into rotational energy by the runner and transmitted through the shaft to the power generator, which produces electrical energy. The residual kinetic energy at the runner outlet is transformed into pressure energy in the draft tube, composed of the cone, elbow, and diffuser, and then the flow is released in the downstream reservoir.

The investigated case corresponds to the scale model of the Francis turbines of high specific speed, $\nu=0.56$ ($n_q=88$) of a hydropower plant built in 1926, owned by ALCAN. The 4.1 m diameter runners of the machines were upgraded in the late a 80s.

Table 1 Measurement chart for $\psi=1.18$ and $\varphi=0.26$ operating point

| $\sigma$ | | | | | $\tau/T$ | | | | | $f/n$ |
|---|---|---|---|---|---|---|---|---|---|---|
| 1.180 | 0.38 | 0.44 | 0.50 | 0.56 | 0.61 | 0.65 | 0.69 | 0.75 | 0.81 | 0.300 |
| 0.780 | | | | | 0.61 | | | | | 0.300 |
| 0.650 | | | | | 0.61 | | | | | 0.300 |
| 0.630 | | | | | 0.61 | | | | | 0.300 |
| 0.600 | | | | | 0.63 | | | | | 0.300 |
| 0.520 | | | | | 0.63 | | | | | 0.309 |
| 0.380 | | | 0.46 | 0.53 | 0.60 | 0.68 | 0.73 | 0.78 | 0.83 | 0.360 |
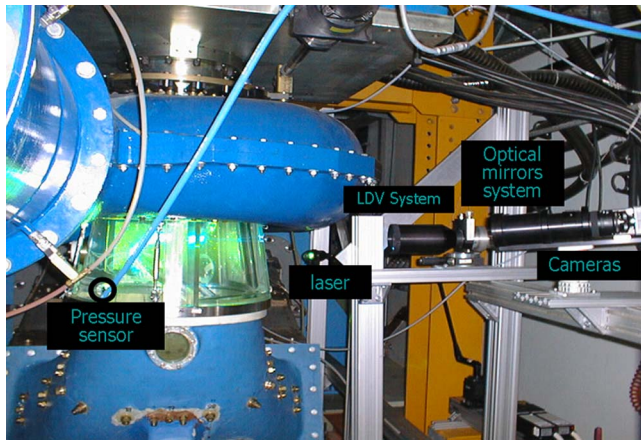
**Fig. 3 Two-phase PIV setup for measuring in the diffuser cone of the Francis turbine scale model**



**Fig. 4 Waterfall diagram of the power spectra of the wall pressure fluctuations in the diffuser cone**

The elbow draft tube of the scale model turbine was especially designed for the purpose of the Flow Investigation in Draft Tubes, FLINDT Research Project EUREKA 1625, see Avellan [17].

The scale model is installed on the third test rig of the EPFL Laboratory for Hydraulic Machines and the performance tests are carried out according to the IEC 60193 standards [18].

## 3 Two-Phase Particle Image Velocimetry Measurements

**3.1 Particle Image Velocimetry System for Two-Phase Flow Measurements.** The PIV measurements have been performed with a Dantec M.T. system. The pulsed light sheet with a thickness of 3 mm is generated by two double-cavity Yttrium aluminum garnet (Nd:YAG) lasers delivering 60 mJ per pulse. An optical high power light guide is used for the positioning of the light sheet in the diffuser cone. Two charge coupled device (CCD) HiSense PIV cameras are used to visualize the illuminated zone, with a series of paired images acquired with a $150-200$ $\mu$s time delay. The camera resolution is $1280 \times 1024$ pixels$^2$ for a $0.20 \times 0.14$ m$^2$ spatial domain. The measurement zone is located at the runner outlet, in the cone of the turbine, see Fig. 6.

To focus the two cameras on the same zone, an optical mirror system is used, Fig. 3. The first camera uses a $532 \pm 15$ nm antireflection-coated filter, focused on the laser wavelength, and the second camera has a cutoff filter ($>570$ nm) on the emission wavelength of fluorescent particles (RhB-580 nm). The two cameras are synchronized with the luminous flashes and then simultaneously exposed. The vector processing is performed with a FlowMap 2200 PIV specific processor, based on an 8 bit resolution cross-correlation technique. The shape of the vortex rope is determined through image processing from the first camera and the unsteady velocity field is obtained from the second one.

**3.2 Particle Image Velocimetry Calibration.** From the measuring field to the camera, the optical path encounters three media of different optical indices: water, polymethylmethacrylate (PMMA), and air. For minimizing the optical distortion of the images and of the laser sheet plane, the diffuser cone windows are manufactured with flat external walls, in front of the cameras and the incident laser light sheet. However, due to the conical internal surface of the draft tube cone, the image distortions remain important. Therefore, they need to be corrected through a calibration procedure, even for this 2D measurement setup.

The calibration consists in defining the coefficients of a transfer function, either linear or nonlinear, that correlates the spatial coordinates in the object plane with the corresponding positions in the 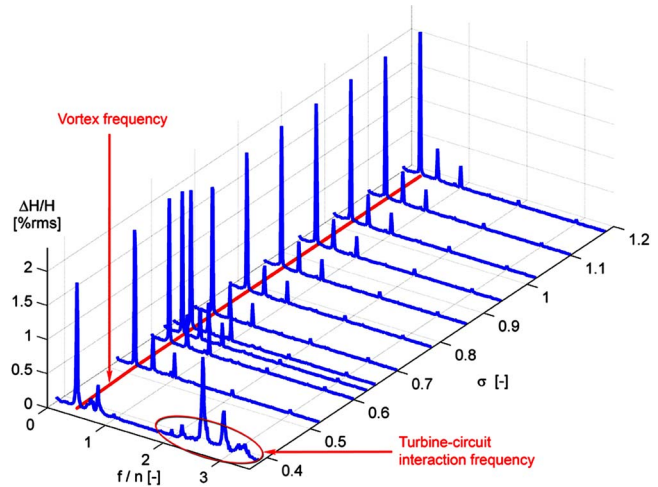recording plane. This transformation integrates the geometrical and optical characteristics of the camera setup, the perspective distortion, lens flaws, and the different media refractive indices, see Soloff et al. [19]. By acquiring images of a target with markers of well-specified spatial position, their corresponding positions in the image plane are known, and thus the geometrical transform matrix coefficients can be determined through a least squares fitting algorithm. The present measurement configuration uses a third-order polynomial function.

The calibration is performed by placing a 2D target of 200 $\times 200$ mm$^2$ with $40 \times 40$ black dots on a white background in the measurement plane position. The test section is then filled with water for reproducing the optical configuration during measurements. The cameras are focused on the target, the calibration images are acquired, and the laser sheet is aligned with the target surface. The target is removed without modifying the optical arrangement. The accuracy of the optical arrangement after the target removal is verified by checking that the particles do not appear blurred on the image.

The estimated uncertainty for the velocity field measurement is less than 3% and it has been checked by comparing the velocity measurement obtained by both PIV and laser Doppler velocimetry (LDV), see Iliescu et al. [20].

**3.3 Particle Image Velocimetry Synchronization.** The rope has a 3D helical shape, see Fig. 1. A conditional sampling of the image acquisition is necessary to reconstruct the spatial position of the rope. The frequency of rope precession is influenced by the $\sigma$ value, see Fig. 4 and Table 1, and can change over a revolution in certain operating conditions. Therefore, the triggering system cannot be based on the runner rotation.

The technique to detect the rope precession is based on the measurement of the pressure pulsation generated at the cone's wall by the precession of the rope. It has the advantage of working even for cavitation-free conditions when the rope is no longer visible, see Ciocan et al. [10], and for this reason, it has been selected as trigger for the PIV data acquisition. The pressure signal power spectra corresponding to the $\sigma$ values are given as a waterfall diagram in Fig. 4. It can be seen that the frequency of the rope precession is decreasing with the $\sigma$ value for this operating point.

As the PIV acquisition is based on the spatial position of the rope, it was necessary to validate correspondence between the wall pressure pulsation and the spatial position of the rope. For this, a second technique based on the optical detection of the rope passage with a LDV probe was used. By reducing the gain, the photomultiplier of the LDV system delivers a signal each time the rope boundary intersects the LDV measuring volume. The posi-

tion of the measurement volume has been chosen close to the wall, to avoid receiving multiple signals over the same revolution, in case the rope crosses the laser beams. The wall pressure signal acquired in parallel allowed referring the rope position to the pressure signal.

Consequently, the image acquisition is triggered with the wall pressure signal breakdown given by the vortex passage. The PIV acquisition is performed at a constant phase delay value with respect to the vortex trigger signal. The influence of the vortex period variation for this kind of phase average calculation is checked and fits within the same uncertainty range as the measurement method 3%, see Ciocan et al. [10].

## 4  Data Processing

**4.1  Image Processing.** The two cameras' images are processed separately. The Camera 1 images are processed to extract the rope characteristics (position and diameter) and Camera 2 image to extract the velocity fields.

The vortex core boundary is irregular, due to vapor compressibility and pressure field fluctuations in the draft tube, which deform the vapor volume. The laser light is unevenly scattered backward and sideways at the water-vapor interface and it gives a strongly illuminated area on images from the first camera. Furthermore, the part of the rope passing in front of the laser sheet, toward the camera, is present on the image, but at a lower gray intensity. This entity also obstructs the field of view of the second camera, and fluorescent particles present in the laser plane, behind the rope, do not appear on the images used for velocity processing. Thus, a digital mask must be applied on each individual vector field for eliminating the outliers in this region.

Due to the topology of the rope, the gray intensity distribution varies drastically on the images from the first camera. In this context, an adaptive image-processing algorithm has been conceived for detecting the geometrical parameters of the rope crossing the measurement plane (see Fig. 5). The distortion correction is performed with the calibration transform prior to image processing.

Several steps are considered for enhancing the quality of the raw grayscale image:

- The image is reduced to the zone occupied by the rope, removing the excess area, which leads to improvement of the grayscale distribution;
- The gray intensity levels are balanced in the image by histogram equalization;
- The noise is removed by nonlinear adaptive bandpass filtering of the image on sliding neighborhoods of $8 \times 8$ pixels;
- The brightness is amplified by histogram shifting toward higher values, weighted logarithmically.

Starting from the improved and uniform quality images, the next step is to detect the rope shape and its dimensions at the intersection between the laser sheet and the rope.

An adaptive threshold is applied on the enhanced grayscale image, for separating the area with concentrated high intensity values from the rest, thus obtaining the position of the zone where the laser sheet crosses the rope boundary.

In parallel, another adaptive threshold is applied on the histogram of the grayscale image for separating the rope shape from the dark background in a binary image. The accuracy of the rope shape detection depends on the gray level gradient between the rope and the background. The position of the rope edge can vary with less than $1\% R_{in}$ and this is the spatial uncertainty of the rope contour. The local minima (holes) on the binary image are filled for smoothing the rope contour. The various white spots of small area are filtered and only the shape with the largest area is kept for further processing. The boundary of this area represents the edge of the rope in the measurement plane. This area is also used like a
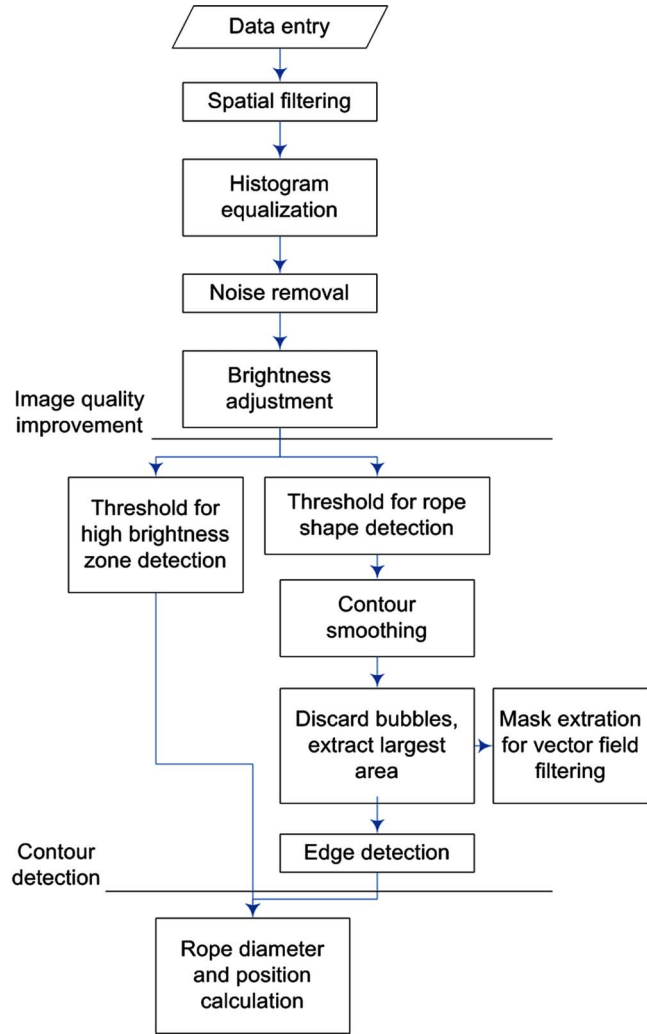


**Fig. 5  Image-processing flowchart**

digital mask for filtering the outliers in the velocity field.

A circular cross section of the rope was assumed throughout this evaluation. Thus, the intersection between the rope and the measurement plane is an elliptical contour. The parameters of the ellipse depend on the local geometrical characteristics of the conical rope helix (angle of incidence, local curvature radius, opening angle of the conical supporting surface). The best approximation of the real rope diameter in our case is the distance between the edges of the rope along a 45 deg direction, applied on the rope intersection with the measurement plane previously obtained. For a variation of the angle with $\pm 10$ deg, the induced error on the rope diameter is $2\% R_{in}$.

An example of a raw image superposed on the rope shape and the rope diameter obtained by image processing is presented in Fig. 6. A detailed description of the image-processing steps is given by Iliescu [21].

Then for each image, the rope center position and the rope diameter are available with an uncertainty of $2\% R_{in}$. The aberrant images are filtered on criteria of minimum/maximum dimension of the rope area and rope diameter. The rate of validated images is 95%.

**4.2  Velocity Field Processing.** For the Camera 2 image, the distortions of position coordinates and particle displacements are corrected through the calibration transform.

For the velocity field calculation, in order to eliminate the outliers in the region of the rope or due to the residual bubbles
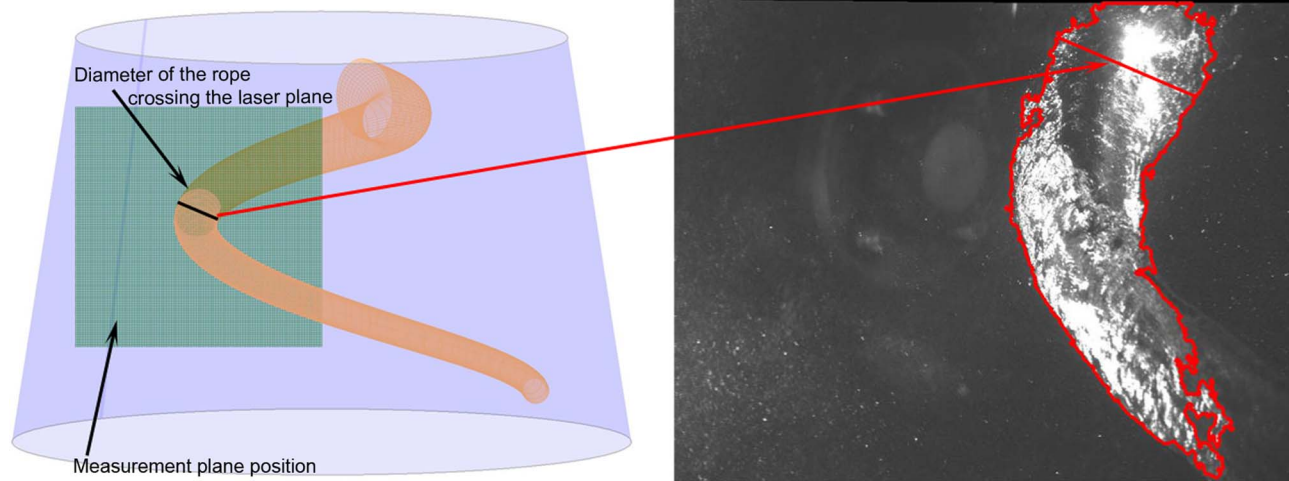
**Fig. 6  Extraction of the rope diameter by image processing from each instantaneous image**

shadow, a mask previously obtained by the image processing of the Camera 1 image is applied on the Camera 2 image. The raw vector maps are processed by cross correlation of the two frames from this masked image of the second camera. The results are filtered by range (vectors four times higher than the mean value are rejected) and peak (the relative height of the highest cross-correlation peak compared to the second highest is chosen 1.2) validation criteria. An example of velocity field is presented in Fig. 7; the instantaneous velocity field is superposed on the raw image for illustration. Statistical convergence is acquired with 1200 velocity fields for 3% uncertainty.

## 5  Flow Analysis

**5.1  Velocity Phase Average.** By ensemble averaging on phase of the instantaneous velocity fields, the mean velocity field is obtained in relation to the phase of the rope precession and for different volumes of the rope corresponding to $\sigma$ values between 0.380 and 1.180. Assuming that the rope shape and the corresponding flow field remain constant over one revolution, the phase of the rope corresponds to its spatial angular position and the spatial velocity field can be reconstructed accordingly, see Fig. 8.
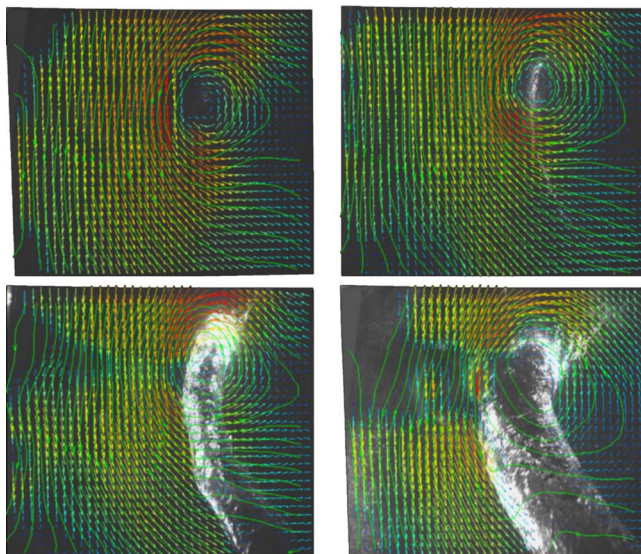


**Fig. 7  Streamlines on instantaneous velocity fields for the same corresponding phase $\tau/T \sim =0.61$ and different $\sigma$ values**

The vortex structure is present for all the investigated $\sigma$ values, and the core of this vortex, with a low pressure area set by the $\sigma$ level, is cavitating and hence determines the rope volume. The cavity volume influences the flow field only locally.

As discussed by Ciocan et al. [10], the average flow velocity shows the decelerated swirling flow that develops in the central stagnation zone. The vortex encloses this zone of average velocity near zero.

The phase average velocity distribution is very similar for all $\sigma$ values. While the flow rate is the same, the influence of the rope volume on the mean velocity field is comparable with the measurement uncertainty. Thus, in phase average, the flow structure is the same for all $\sigma$ values, but a local modification of the velocity field and turbulent kinetic energy field in the near vicinity of the rope is expected. Unfortunately, for the moment, it is difficult to analyze this zone due to the lack of uncertainty near the rope boundary region, and strong and random reflections as well as shadows at the intersection of the rope with the laser sheet are observed.

**5.2  Vortex Centerline for the Cavitation-Free Configuration.** For the cavitation-free configuration, see Fig. 7 for $\sigma=1.180$, the vortex center is detected starting from the velocity field analysis. Four methods are commonly used, see Sadarjoen et al. [22], to detect its position:

- minimum of velocity
- streamline curvature centers density
- maximum of vorticity $|\nabla \times \mathbf{C}|$
- maximum of normalized helicity $\mathbf{C}\nabla \times \mathbf{C}/|\mathbf{C}||\nabla \times \mathbf{C}|$

In swirling flows, the main contribution to the vorticity is given by the mean tangential and axial components, and the vorticity profile is significant in the plane normal to the vortex filament. For the instantaneous velocity fields, the vorticity calculation is very sensitive to the relative position of the vortex and measurement plane. Consequently, computing the vorticity distribution only with the two measured velocity components does not have the proper physical meaning, nor has the helicity.

Due to the unsteadiness of the flow, an instantaneous velocity field may present zones of low velocity outside the vortex center zone. Thus, the minimum of velocity criterion, easy to implement, is not relevant in this case.

The second method, streamline curvature center density, is more consistent. By the streamline generation in each gridpoint, for each unsteady vector field, we compute the curvature centers of the streamlines, and the regions with high density of curvature centers indicate the presence of a vortex center. The center posi-
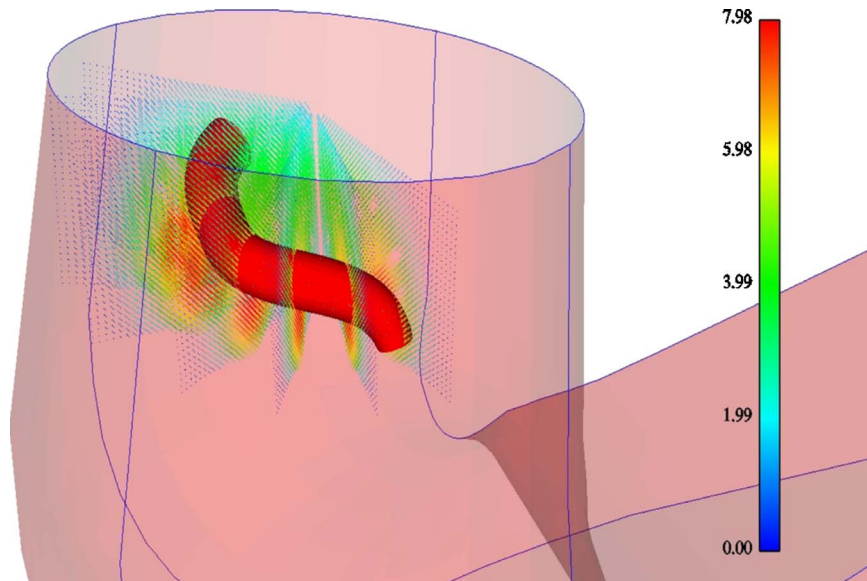
Fig. 8 Phase averaged vectors field for $\sigma=0.380$

tion is given by the mean of the curvature centers coordinates.

To speed up the computation time for the center detection, a combination of these two criteria has been used as vortex center-tracking algorithm. The streamline generation is performed only in the regions where the minimum velocity is obtained. The second method is applied afterwards to detect the vortex center. An instantaneous result, obtained by these two methods, see Fig. 9, shows a very good coherence of the center position within the measurement resolution range. The validation rate on instantaneous fields, based on coherent position criteria, is higher than 99%.

**5.3 Rope Contour Phase Average.** Starting from each image-processing result, for each rope precession phase and each $\sigma$ value, the ensemble averaging by phase of the rope shape is performed, and thus the rope characteristics (position and diameter) in the measurement plane are determined.

Assuming that the angular velocity of the rope is constant over a rope revolution, i.e., assuming a solid body rotation of the rope, the rope precession temporal phase is transposed into angular position. In this way, the spatial position of the rope core is reconstructed in the turbine cone, see Fig. 10. Adding the measured diameters, in a plane normal to the core, leads to rendering the 3D rope shape, see Fig. 11.

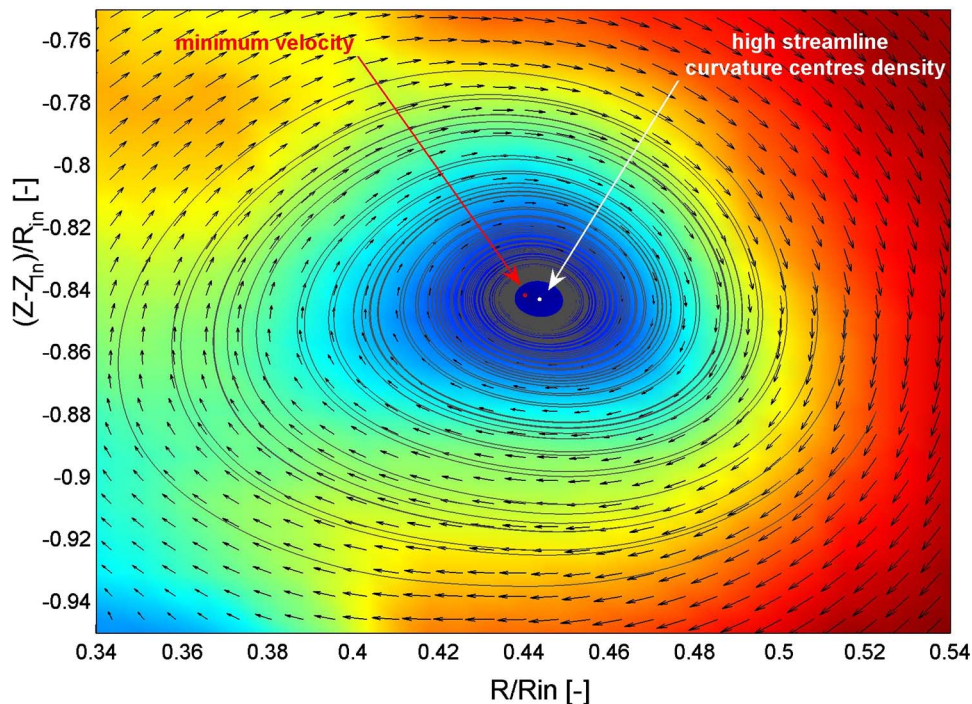For the same $\sigma$ value, the rope center position and the mean



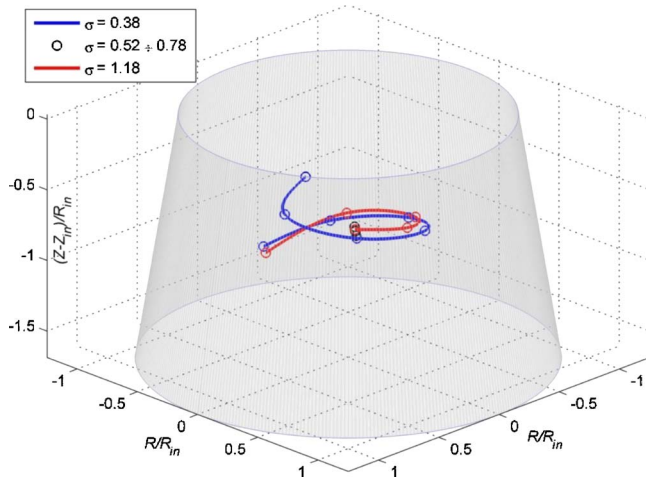Fig. 9 Vortex center detection for noncavitating conditions

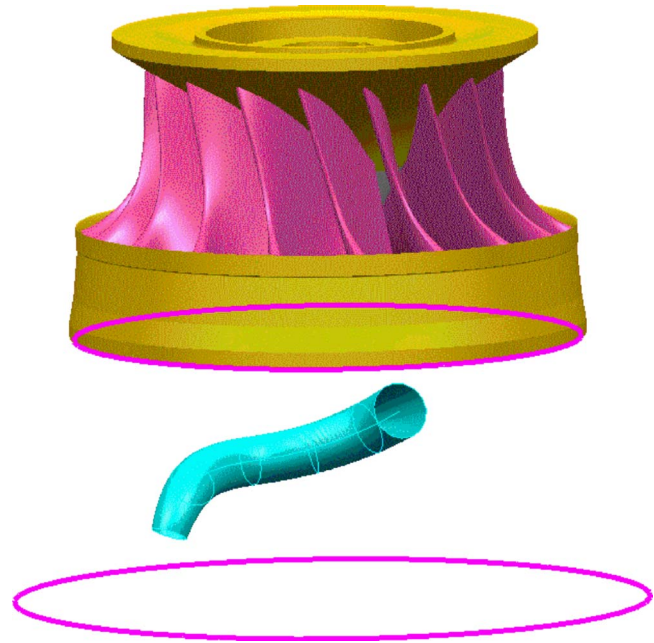Fig. 10 Vortex centerlines for $\sigma=0.380$ and $\sigma=1.180$

value of the rope diameter are calculated, and the corresponding standard deviations are estimated for the entire measurement zone, See Fig. 12.
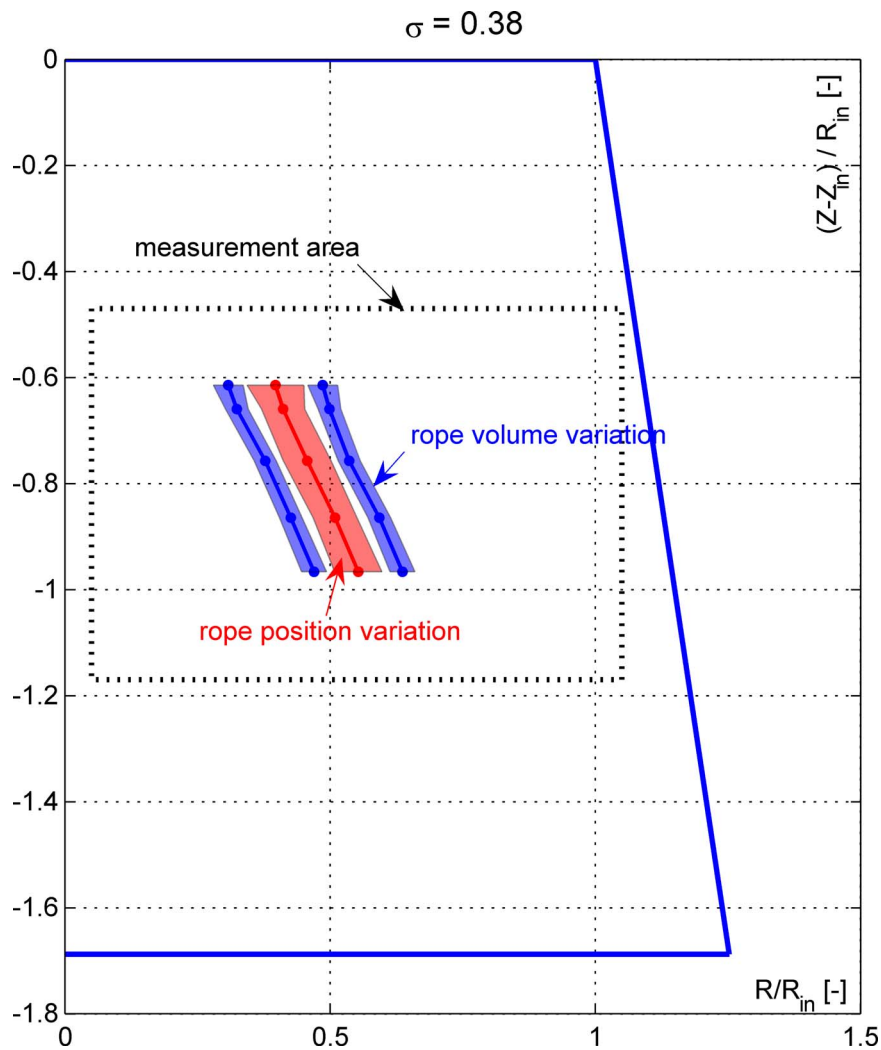


Fig. 11 Reconstruction of the rope volume



Fig. 12 Standard deviation of the rope position and rope volume
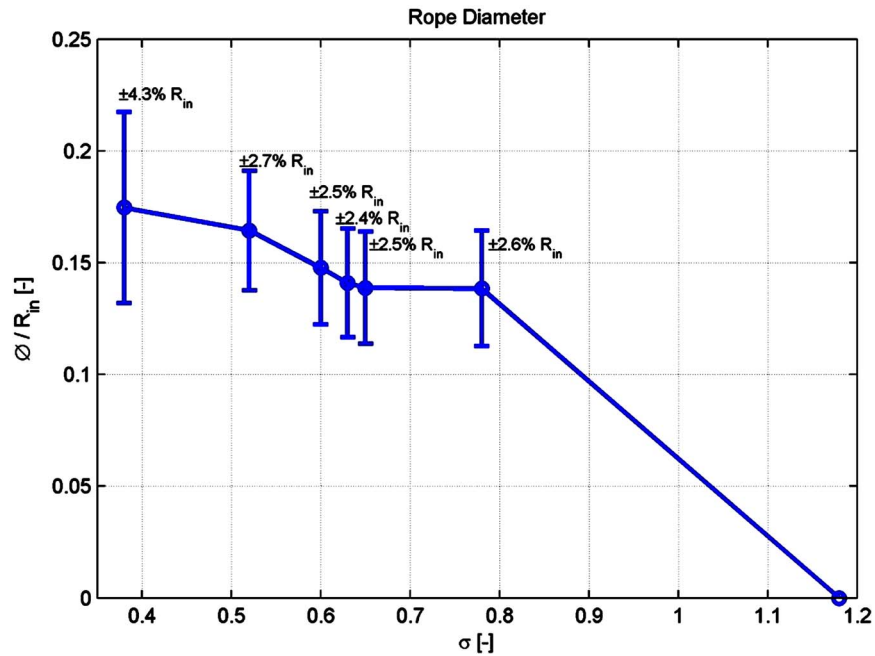
**Fig. 13 Rope diameter variations versus the σ value**

**5.4 Flow Behavior Corresponding to σ Variation.** The procedure to determine the geometrical parameter of the rope in phase average, already described, is applied for seven σ values. The rope diameters as well as the rope center position in the measurement zone are represented versus the σ value. Associated with these values, the standard deviations of the rope diameter and vortex center position are calculated, see Fig. 13.

The rope diameter decreases from low to high σ values. The standard deviation of the rope diameter is related to the rope diameter fluctuations and is a measure for the rope volume variation. This calculation is physically significant due to the axial pressure waves that act on the vapor cavity, resulting in a volume variation under the influence of the local change of pressure dis-

tribution. The standard deviations are quasiconstant for all σ values at 2.5% of $R_{1e}^-$, except for the value 0.380, where it increases at 4.3% of $R_{1e}^-$, see Fig. 13. For $σ=0.380$, the rope area referred to the local cone section area has a variation between 0.5% and 1.2%.

In fact, for the $0.380σ$ value, it was demonstrated by hydroacoustic simulation, see Nicolet et al. [23], that a pressure source located in the inner part of the draft tube elbow induces a forced excitation. This excitation represents the synchronous part of the vortex rope excitation. An eigenfrequency of the hydraulic system is also excited at 2.5 fn, see Fig. 4, and the plane waves, generated by the pressure source, propagate in all the hydraulic circuit. The
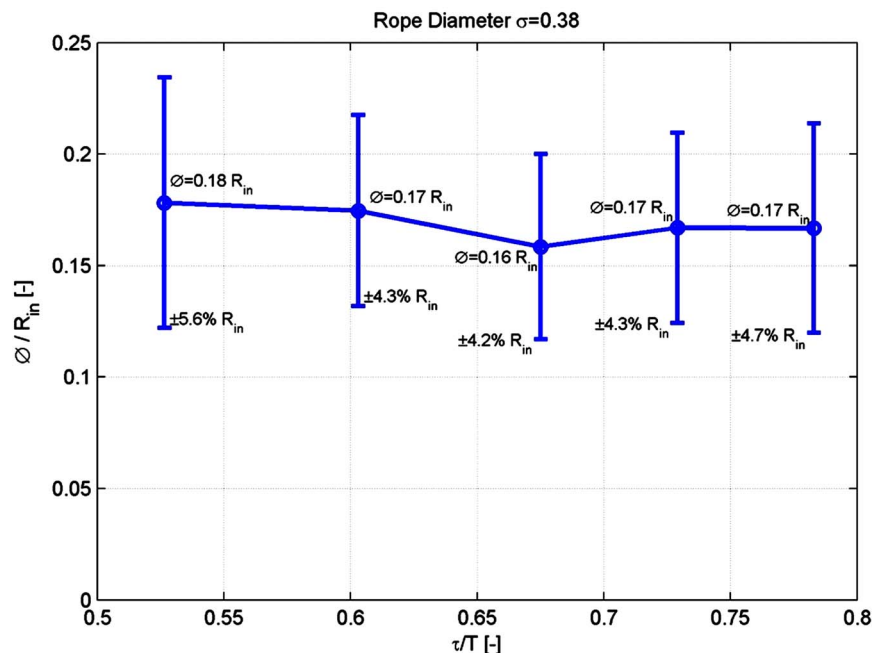


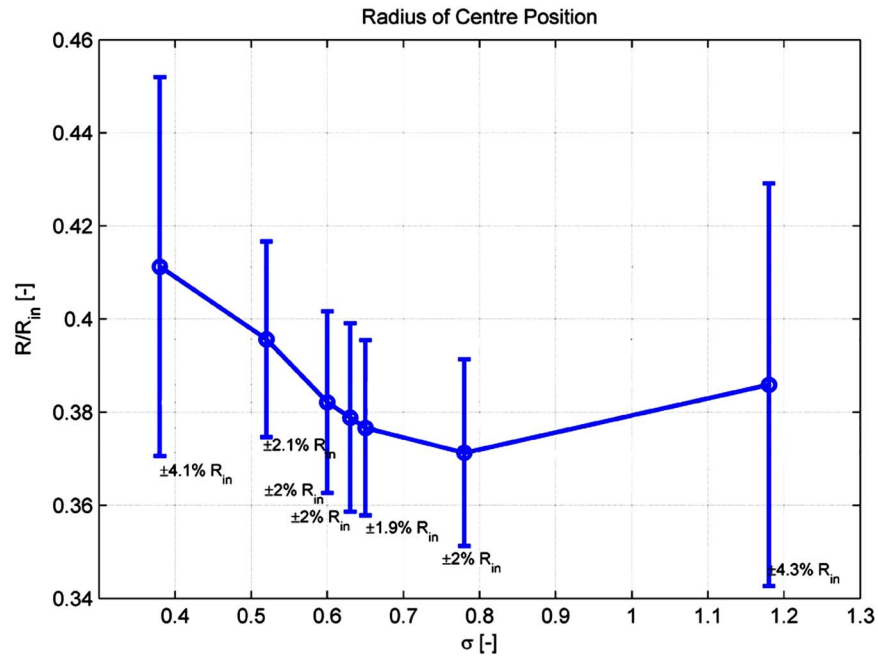**Fig. 14 Rope diameter variations versus the vortex phase τ**

**Fig. 15  Rope center variations versus the $\sigma$ value**

passing of the plane waves in the rope section induces successively an expansion and a contraction of the vapor volume of the rope, which explains the increase of the rope diameter standard deviation for this $\sigma$ value.

For the lowest $\sigma$ value, the rope diameter and its standard deviation remain virtually unchanged (the change is smaller than the measurement uncertainty) with respect to the precession phase angle over the measured domain, see Fig. 14.

The vortex center position is nearly constant between low $\sigma$ values and cavitation-free conditions, see Fig. 15. For low $\sigma$ values, the eccentricity of the rope position—the position of the rope center related to the cone symmetry axis—increases and thus the

pressure amplitude fluctuation at the wall increases too, see Fig. 4. The standard deviation of the vortex center position is representative of the flow stability. For $\sigma=0.380$, the location of the rope center has an unsteady spatial variation of $\sim 8\%$ of the local radius of the cone. The resonance at this $\sigma$ value induces a loss of stability of the rope position highlighted by the increase of the standard deviation of the vortex center position, i.e., it doubles from 2% to 4.1% $R_{in}$, except for the value 0.380, where it increases at 4.3% of $R_{in}$.

In the cone cross section, the rope center eccentricity (the radius of the rope center) increases following the phase evolution:
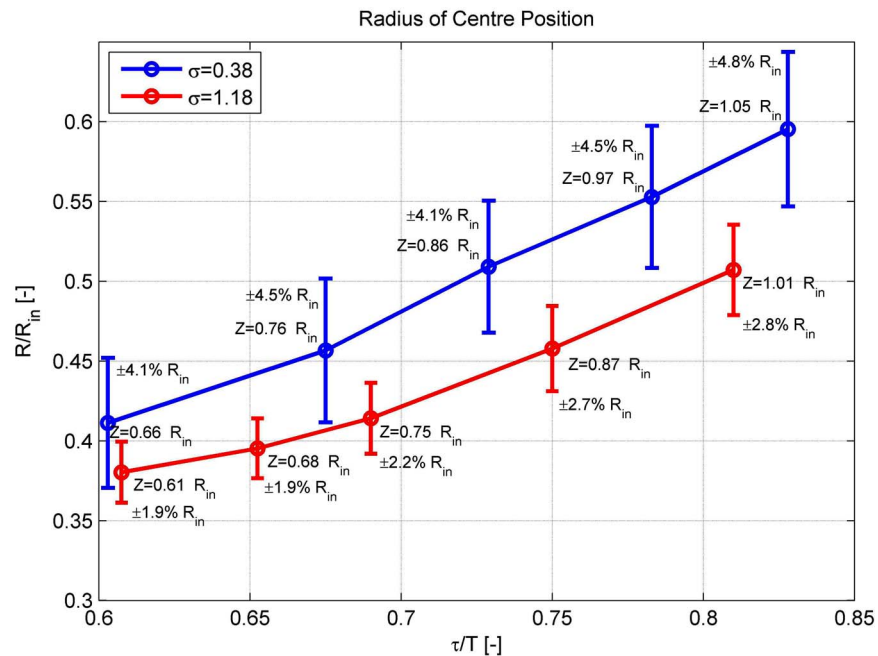


**Fig. 16  Vortex position variations for $\sigma$1.180 and 0.380 values versus the vortex phase $\tau$**

the rope goes closer to the wall downstream in the cone. This evolution induces the increase of the wall pressure fluctuation synchronous with the rope rotation. The standard deviation corresponding to the rope position is quasiconstant for all phases (depth) in the measurement zone, see Fig. 16.

## 6 Conclusions

The PIV system gives the opportunity to survey the flow velocity field in the diffuser cone of a scale model of a Francis turbine at part load operating conditions with a precessing cavitation rope. From the experimental results, the complete description and quantification of the velocity, simultaneously with the rope boundary behavior, were obtained for different cavitation conditions.

The synchronization of the PIV acquisition with the rope position allows, by ensemble averaging, the reconstruction of the rope volume in correlation with the corresponding velocity field, in the cone of the turbine model. Image processing provides an estimation of the rope diameter and the positions of the vortex center in the measuring zone.

For a particular $\sigma$ value that corresponds to a coincidence of the rope excitation with an eigenfrequency of the hydraulic circuit, the influence of the pressure source on the rope dynamics is shown.

An experimental database has been built and is now available for future validation of analytical modeling and numerical simulation of draft tube flows.

## Acknowledgment

## Nomenclature

BEP = best efficiency operating point
$C$ = mean absolute velocity (m/s)
$C_p$ = pressure coefficient $C_p = (p - \bar{p})/1/2\rho c_{m1}^2$ (-)
$C_{\text{ref}}$ = mean flow reference velocity $C_{\text{ref}} = Q/\pi R_{\text{in}}^2$ (m/s)
$\bar{D}_{1e}$ = runner diameter (m)
$E$ = specific energy (J/kg)
$f_c$ = vortex rotation frequency (Hz)
$Q$ = flow rate (m$^3$/s)
$Q_{\text{BEP}}$ = flow rate at the best efficiency operating condition (m$^3$/s)
$k$ = turbulent kinetic energy (m$^2$/s$^2$)
$f_n$ = runner rotation frequency (Hz)
NPSE = net positive suction specific energy (J/kg)
$R$ = local cone radius (m)
$R_{\text{in}}$ = runner outlet radius (m)
$Z$ = current cone elevation (m)
$Z_{\text{in}}$ = runner outlet elevation (m)
$\Delta Z$ = cone height (m)
$\omega$ = rotational angular velocity (rad/s)
$\Phi$ = local rope diameter (m)

$\psi$ = specific energy coefficient (-)
$\varphi$ = flow rate coefficient (-)
$\sigma$ = thoma number $\sigma = \text{NPSE}/E$ (-)
$\theta$ = vortex polar angle $\theta = 2\pi f_c \tau$ (rad)
$\tau$ = rope phase (rad)

## References

[1] Jacob, T., 1993, "Evaluation sur Modèle Réduit et Prédiction de la Stabilité de Fonctionnement des Turbines Francis," thesis, EPFL, Lausanne.
[2] Arndt, R., 2002, "Cavitation in Vortical Flows," Annu. Rev. Fluid Mech., **34**, pp. 143–175.
[3] Alekseenko, S. V., Kuibin, P. A., Okulov, V. L., and Shtork, S. I., 1999, "Helical Vortices in Swirl Flow," J. Fluid Mech., **382**, pp. 195–243.
[4] Okulov, V. L., 1995, "The Velocity Field Induced by Helical Vortex Filaments With Cylindrical or Conical Supporting Surface," Russ. J. Eng. Thermophys., **5**, pp. 63–75.
[5] Wang, X., Nishi, M., and Tsukamoto, H., 1994, "A Simple Model for Predicting the Draft Tube Surge," Proceedings of the 17th IAHR Symposium, Beijing, China, Sept. 15–19, Vol. 1, pp. 95–106.
[6] Philibert, R., and Couston, M., 1998, "Matrix Simulating the Gaseous Rope," Proceedings of the 19th IAHR Symposium (), Singapore, Sept. 9–11, Vol. 1, pp. 441–453.
[7] Hocevar, M., Sirok, B., and Blagojevic, B., 2005, "Prediction of Cavitation Vortex Dynamics in the Draft Tube of a Francis Turbine Using Radial Basis Neural Network," Neural Comput. Appl., **14**, pp. 229–234.
[8] Zhang, R. K., Cai, Q. D., Wu, J. Z., Wu, Y. L., Liu, S. H., and Zhang, L., 2005, "The Physical Origin of Severe Low-Frequencies Pressure Fluctuations in Giant Francis Turbines," Mod. Phys. Lett. B, **19**(28–29), pp. 99–102.
[9] Susan-Resiga, R., Ciocan, G. D., Anton, I., and Avellan, F., 2006, "Analysis of the Swirling Flow Downstream a Francis Turbine Runner," ASME J. Fluids Eng., **128**, pp. 177–189.
[10] Ciocan, G. D., Iliescu, M. S., Vu, T., Nennemann, B., and Avellan, F., 2007, "Experimental Study and Unsteady Simulation of the FLINDT Draft Tube Rotating Vortex Rope," ASME J. Fluids Eng., **129**, pp. 146–158.
[11] Paik, J., Sotiropoulos, F., and Sale, M. J., 2005, "Numerical Simulation of Swirling Flow in Complex Hydroturbine Draft Tube Using Unsteady Statistical Turbulence Models," J. Hydraul. Eng., **131**(6), pp. 441–456.
[12] Adrian, R. J., 2005, "Twenty Years of Particle Image Velocimetry," Exp. Fluids, **39**, pp. 159–169.
[13] Kadambi, J. R., Charoenngam, P., Subramanian, A., Wernet, M. P., Sankovic, J., Addie, G., and Courtwright, R., 2004, "Investigations of Particle Velocities in a Slurry Pump Using PIV: Part 1, The Tongue and Adjacent Channel Flow," ASME J. Energy Resour. Technol., **126**, pp. 1–9.
[14] Dias, I., and Riethmuller, M. L., 1998, "Visualisation of the Forming Bubble and PIV Measurement of Surrounding Liquid Using Fluorescent Particles," Proceedings of Eigth International Symposium of Flow Visualisation, Sorrento, Italy.
[15] Lindken, R., and Merzkirch, W., 2000, "Velocity of Liquid and Gaseous Phase for a System of Bubbles Rising in Water," Exp. Fluids, **29**(7), pp. 194–201.
[16] Lindken, R., and Merzkirch, W., 2002, "A Novel PIV Technique for Measurements in Multiphase Flows and Its Application to Two-Phase Bubbly Flows," Exp. Fluids, **33**, pp. 814–825.
[17] Avellan, F., 2000, "Flow Investigation in a Francis Draft Tube: The FLINDT Project," Proceedings of 20th I. A. H. R. Hydraulic Machinery and Systems, Charlotte, No, Aug. 7–9, Vol. 1, Paper No. DES-11.
[18] IEC 60193 Standard, 1999, "Hydraulic Turbines, Storage Pumps and Pump-Turbines-Model Acceptance Tests," International Electrotechnical Commission, Genève, Nov.
[19] Soloff, S. M., Adrian, R. J., and Liu, Z.-C., 1997, "Distortion Compensation for Generalized Stereoscopic Particle Image Velocimetry," Meas. Sci. Technol., **8**, pp. 1441–1454.
[20] Iliescu, M. S., Ciocan, G. D., and Avellan, F., 2004, "Experimental Study of the Runner Blade-to-Blade Shear Flow Turbulent Mixing in the Cone of Francis Turbine Scale Model," Proceedings of the 22nd IAHR Symposium on Hydraulic Machinery and Systems, Stockholm, Sweden, Jun. 29–Jul. 2.
[21] Iliescu, M. S., 2007, "Large Scale Hydrodynamic Phenomena Analysis in Turbine Draft Tubes," thesis, EPFL, no. 3775, Lausanne.
[22] Sadarjoen, A. I., Post, F. H., Ma, B., Banks, D. C., and Pagendarm, H.-G., 1998, "Selective Visualization of Vortices in Hydrodynamic Flows," Proceedings of IEEE Visualization, Los Alamitos, CA, Oct. 18–23.
[23] Nicolet, C., Arpe, J., and Avellan, F., 2004, "Identification and Modeling of Pressure Fluctuations of a Francis Turbine Scale Model at Part Load Operation," Proceedings of the 22nd IAHR Symposium on Hydraulic Machinery and Systems, Stockholm, Sweden, Jun. 29–Jul. 2.